Eur Radiol (2017) 27:985–994
DOI 10.1007/s00330-016-4433-0

MAGNETIC RESONANCE

Feasibility of self-gated isotropic radial late-phase MR imaging of the liver

Jakob Weiss[1] · Jana Taron[1] · Ahmed E. Othman[1] · Robert Grimm[2] · Matthias Kuendel[1] · Petros Martirosian[1] · Christer Ruff[1] · Christina Schraml[1] · Konstantin Nikolaou[1] · Mike Notohamiprodjo[1]

Received: 12 January 2016 / Revised: 15 May 2016 / Accepted: 20 May 2016 / Published online: 8 June 2016

Abstract

Objective To evaluate feasibility of a 3D-isotropic self-gated radial volumetric interpolated breath-hold examination (VIBE) for late-phase MRI of the liver.

Material and methods 70 patients were included and underwent liver MRI at 1.5 T. Depending on the diagnosis, either Gd-EOB-DTPA (35 patients) or gadobutrol (35 patients) were administered. During late (gadobutrol) or hepatocyte-specific phase (Gd-EOB-DTPA), a radial prototype sequence was acquired and reconstructed using (1) self-gating with 40 % acceptance ($rVIBE_{40}$); (2) with 100 % acceptance of the data ($rVIBE_{100}$) and compared to Cartesian VIBE (cVIBE). Images were assessed qualitatively (image quality, lesion conspicuity, artefacts; 5-point Likert-scale: 5 = excellent; two independent readers) and quantitatively (coefficient-of-variation (CV); contrast-ratio) in axial and coronal reformations.

Results In eight cases only rVIBE provided diagnostic image quality. Image quality of $rVIBE_{40}$ was rated significantly superior ($p < 0.05$) in Gd-EOB-DTPA-enhanced and coronal reformatted examinations as compared to cVIBE. Lesion conspicuity was significantly improved ($p < 0.05$) in coronal reformatted Gd-EOB-DTPA-enhanced $rVIBE_{40}$ in comparison to cVIBE. CV was higher in $rVIBE_{40}$ as compared to $rVIBE_{100}$/cVIBE ($p < 0.01$). Gadobutrol-enhanced $rVIBE_{40}$ and cVIBE showed higher contrast-ratios than $rVIBE_{100}$ ($p < 0.001$), whereas no differences were found in Gd-EOB-DTPA-enhanced examinations.

Conclusion Self-gated 3D-isotropic rVIBE provides significantly superior image quality compared to cVIBE, especially in multiplanar reformatted and Gd-EOB-DTPA-enhanced examinations.

Key Points

- *Radial VIBE acquisition reduces motion artefacts.*
- *Gd-EOB-DTPA-enhanced scans provide improved image quality.*
- *Non-diagnostic liver MRI examinations may be reduced by radial k-spaces sampling.*

Keywords Magnetic resonance imaging · Radial VIBE · Gd-EOB-DTPA · Artefacts · Liver

Introduction

Magnetic resonance imaging (MRI) is the mainstay of liver imaging [1–3], but impairment of image quality due to motion artefacts, particularly in the phase-encoding direction, remains a limiting problem [4, 5]. Especially in children, the elderly and critically ill patients who are unable to perform a sufficient breath-hold, the number of non-diagnostic examinations is high [6, 7]. The recently introduced radial k-space readout technique using the stack-of-star scheme is a promising alternative to overcome this problem [8]. First described in 1973 by Lauterbur, this data acquisition technique failed early clinical implementation because of a variety of technical problems such as magnetic field heterogeneity and the lack of precise time-varying gradient fields [9]. By solving these issues in recent years, radial k-space readout sequences have been

✉ Jakob Weiss
Jakob.Weiss@med.uni-tuebingen.de

[1] Department of Diagnostic and Interventional Radiology, Eberhard Karls University Tuebingen, Hoppe-Seyler-Straße 3, 72076 Tuebingen, Germany

[2] Siemens Healthcare MR, Erlangen, Germany

established in clinical routine as a motion-insensitive alternative to conventional sequences with Cartesian read-out [10]. The underlying principles are that the in-plane (kx; ky) read-out is performed along rotated spokes whereas the sampling along the slice direction (kz) follows the conventional Cartesian data acquisition [10–12]. The resulting spoke overlap in the centre of the data set prevents the appearance of ghosting artefacts and has a motion-averaging effect, thus allowing for a more motion-robust data acquisition. Promising results have already been described for various body parts depending on respiratory motion [12–16]. Although motion artefacts can be significantly reduced using radial imaging, a remaining problem is the motion-related blurring of the borders of anatomical structures. One possibility to overcome this issue is integration of a recently developed approach using only data acquired during self-gated end-expiration [17, 18]. Moreover, the increased motion robustness allows for 3D-isotropic volumetric data acquisition, which is routinely used in musculoskeletal and brain imaging. This approach provides higher spatial resolution and signal-to-noise ratios, and facilitates multiplanar reformations [19–22]. This seems especially useful for accurate evaluation of liver anatomy and small lesion detection in late-phase acquisitions, particularly in scans enhanced with the hepatocyte-specific contrast agent Gd-EOB-DTPA.

Therefore the purpose of this study was to evaluate the feasibility of free-breathing self-gated 3D-isotropic radial volumetric interpolated breath-hold examination (VIBE) of late-phase liver MR imaging in Gd-EOB-DTPA or gadobutrol-enhanced scans. Our hypothesis was that a free-breathing self-gated 3D-isotropic radial VIBE approach would significantly reduce motion artefacts and provide superior image quality as compared to standard Cartesian VIBE, especially in multiplanar reformations and Gd-EOB-DTPA-enhanced scans.

Materials and methods

Radial k-space read-out sequences are part of our liver standard protocol as radial k-space sampling has become routinely used for abdominopelvic MR imaging [6, 10, 11]. The investigated reconstruction algorithm does not prolong scan time and is performed on a raw data base. Thus the local ethics committee approved the retrospective analysis of the routine clinical data and waived written informed consent.

Patient characteristics

From November 2014 to June 2015, 70 patients divided in two groups (Group A: 35 consecutive patients with Gd-EOB-DTPA-enhanced MRI; Group B: 35 consecutive patients with gadobutrol-enhanced MRI) scheduled for contrast-enhanced (CE) liver MRI were included in this study. All examinations were performed in the setting of clinically suspected or known liver pathologies. Gd-EOB-DTPA-enhanced MRI was performed as baseline examination in subjects with suspected primary hepatic malignancies, e.g. hepatocellular carcinoma (HCC), unclear intrahepatic mass or pathologies of the biliary system. Gadobutrol-enhanced MRI was performed in subjects with suspected hepatic metastasis or follow-up examinations of primary hepatic malignancies. Exclusion criteria were incomplete examinations and patients under the age of 18 years. A summary with detailed patient demographics is provided in Table 1.

Acquisition parameters

All examinations were performed on a whole-body 1.5 T scanner (MAGNETOM Aera, software *syngo* MR D13A, Siemens Healthcare, Erlangen, Germany) using a 50-channel coil setup (body array coil with 18 channels and a 32-channel spine coil) in supine position. As described above, either Gd-EOB-DTPA

Table 1 Demographics of the subjects included in this study

Variables	N; mean ± SD	
Subjects	70	
Group A = Gd-EOB-DTPA	35	
Group B = Gadobutrol	35	
Exclusions (incomplete examination)	2 (n = 1 Group A; n = 1 Group B)	
Age; sex ratio (m/f)	61.3 ± 12.7 [range 36–80]; 37/31	
Clinical diagnosis	Group A	Group B
Hepatocelluar carcinoma	26	8
Colon carcinoma	2	13
Breast cancer	1	6
Melanoma	0	4
Others	5	3

Dinatrium (Primovist/Eovist; Bayer Healthcare) or gadobutrol (Gadovist; Bayer Healthcare) were administered at 0.1 mmol/kg body weight followed by a 20-ml saline flush. Standard CE liver MRI protocol was acquired with axially oriented unenhanced, arterial, portal-venous, interstitial and hepatobiliary scans (20 min post injection; only for Gd-EOB-DTPA) using a standard Cartesian T1-weighted VIBE (cVIBE) with the following acquisition parameters: slice thickness 2.2 mm; matrix 256 × 140; field of view (FOV) 420 × 360 mm^2; in-plane-resolution 1.2 × 1.2 mm^2; TR 3.32 ms; TE 1.24 ms; parallel imaging with GRAPPA factor 2; acquisition time 12 s; phase resolution 70 %; slice resolution 50 %.

T1-weighted radial VIBE (rVIBE) rVIBE was routinely performed directly after the last cVIBE axially under free-breathing conditions. This recently commercially available sequence is based on the lately introduced volumetric k-space readout using the stack-of-stars scheme. The acquisition principles have been described recently in detail [6, 10–12]. In short: conventional Cartesian k-space sampling is only performed along the slice direction (kz) whereas in-plane (kx; ky) readout is performed along rotated spokes (Fig. 2). The resulting spoke overlap in the centre prevents the appearance of ghosting artefacts and has a motion-averaging effect, thus allowing for a more motion-robust data acquisition [10].

The acquisition parameters of this isotropic sequence were as follows: slice thickness 1.4 mm; radial views 800; matrix 256 × 256; 176 slices; FOV 420 × 420 × 360 mm^2; in-plane-resolution 1.4 × 1.4 mm^2; TR 3.63 ms; TE 1.67 ms; no parallel imaging was performed; acquisition time 4–7 min depending on the number of acquired slices due to different liver size. The golden-angle increment of 111.25° was used as rotation angle.

In addition to the standard reconstruction using the complete data set ($rVIBE_{100}$), we applied a prototype raw data reconstruction algorithm ($rVIBE_{40}$) that implements a retrospective self-gating approach and allows sorting of the acquired data into bins according to the respiration phase. Due to the implementation of this algorithm in the standard online reconstruction process, no additional offline reconstruction time is required. The self-gating signal was extracted from the k-space centre $k_x = k_y = k_z = 0$, which is crossed by every radial readout in the central k-space partition ($k_z = 0$). The signal was automatically derived from the receive coil element that showed the most significant contribution in the range of respiratory frequencies but low contamination from respiratory frequencies and noise [16]. For image reconstruction, only 40 % of the acquired data at the most consistently visited respiratory position were used, which is typically close to end-expiration. This gating strategy is also known as optimal gating [23]. The goal of self-gating is to further reduce motion artefacts and blurriness in the radially acquired images. Schemes of the stack-of-stars trajectory and the self-gating algorithm are provided in Fig. 1.

Data analysis

The last cVIBE acquired either during the portal venous or hepatobiliary phase served as standard of reference for rVIBE-sequences. Due to the limited breath-hold capability of the patients, isotropic acquisition of Cartesian VIBE within a breath-hold could not be performed, so that we adhered to the institutional standard sequence, providing an almost isotropic resolution.

Qualitative analysis

All images were appraised on a dedicated workstation (*syngo*.via, A30A; Siemens Healthcare, Erlangen, Germany) by two observers independently blinded to the clinical diagnosis. All ratings used a five-point Likert scale (5 = excellent with well-defined margins; 4 = good with minor deficits; 3 = fair with moderate blurriness; 2 = poor with substantial deficits; 1 = non-diagnostic). Reading scores ≤ 2 comprising

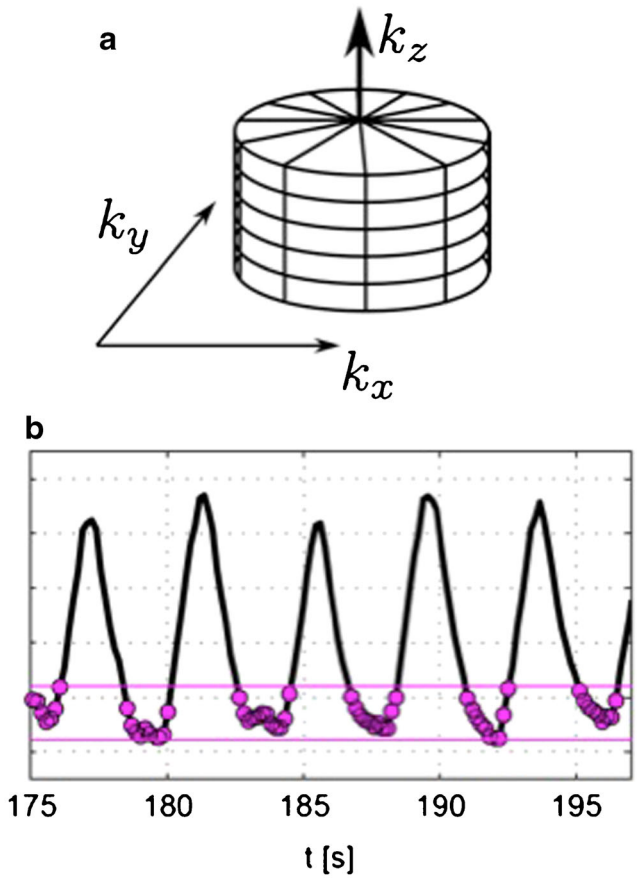

Fig. 1 (**a**) Stack-of-stars acquisition. (**b**) Self-gating signal and accepted samples

all observed parameters were considered as non-diagnostic. Discreet and unclear findings were correlated in multiplanar reformations to confirm or rule out the diagnosis. The final qualitative imaging scores of all assessed parameters were calculated by averaging the individual scores of both readers.

Image quality All readings were performed using axial and coronal multiplanar reformations (*syngo*.via, Siemens Healthcare) comprising four aspects: (1) overall image quality, (2) clarity and sharpness of hepatic vessels and liver edge, (3) focal lesion conspicuity (primary hepatic malignancies and metastases of all sizes were pooled and reading was performed patient-based) and (4) in Gd-EOB-DTPA-enhanced scans, depiction of the biliary tree/common bile duct.

Artefacts We have also recorded impairment due to sequence specific artefacts: (1) Streak artefacts due to radial sampling in rVIBE sequences and (2) motion artefacts in phase sampling direction in cVIBE and rVIBE sequences.

Quantitative analysis

Image homogeneity As we applied parallel imaging techniques in the cVIBE acquisition and different k-space sampling approaches, valid determination of signal- and contrast-to-noise-ratios could not be performed [24]. As a quantitative surrogate for image quality, the coefficient of variation (CV) was calculated to evaluate the homogeneity of the acquired signal and thus describing the degree of variation among the sequences. Calculation was performed as follows:

$$CV = SD_{ROI1} \Big/ Mean_{ROI1}, \quad (1)$$

where SD_{ROI1} is the standard deviation in the region of interest (ROI) and $Mean_{ROI1}$ is the signal intensity of the same ROI. To achieve the most unadulterated results the ROI was placed in the same part and level of most homogeneous liver parenchyma in all acquired sequences.

Liver-to-lesion contrast As a surrogate for CNR, we quantified the depiction of focal liver lesions (biggest lesion if n > 1) by calculating the ratio to visually normal liver parenchyma using the following equation:

$$\text{Contrast } \% = \left\{ \frac{(SI_{RoI1} - SI_{ROI2})}{(SI_{ROI1} + SI_{ROI2})} \right\} \times 100 \quad (2)$$

SI = signal intensity; ROI1 = normal liver tissue; ROI2 = focal liver lesion

Due to the study design, lesion conspicuity was assessed in late-phase (gadobutrol) or hepatocyte-specific phase (Gd-EOB-DTPA) scans. Therefore, Liver-to-Lesion contrast indicates the ratio of contrast-enhanced liver parenchyma to a hypointense focal lesion.

Statistical analysis

All statistical analyses were performed using SPSS Statistics (Version 22, IMB, Armonk, NY, USA). For normally distributed data ANOVA analysis was calculated. For non-parametric data Friedman´s-ANOVA was performed. Multiple comparisons were accounted by using the Bonferroni correction. Comparison of mean values was calculated using the Student's t-test for normally distributed data and the Wilcoxon singed-rank test for non-parametric data, respectively. Inter-reader agreement was determined by calculating weighted kappa. P-values < 0.05 were assumed to indicate statistical significance.

Results

MRI of the liver was successfully completed in 68 subjects (37 male, 31 female; mean age 61.3 ± 12.7). Two subjects (n = 1 Group A; n = 1 Group B) were excluded due to incomplete data acquisition. No exclusions were made because of poor physical conditions or insufficient breath-hold capabilities. For detailed patient demographics see Table 1.

Qualitative image analysis

In eight patients (11.4 %) only the radial VIBE, in particular the self-gated reconstruction provided diagnostic image quality (reading scores ≥3) to detect relevant findings such as discreet liver lesions (n = 7) or portal venous thrombosis (n = 1) whereas the cVIBE was considered non-diagnostic (reading scores ≤ 2) due to severe motion artifacts caused by inadequate breath holding. Figure 2 shows an example where only radial VIBE acquisition provides diagnostic image quality.

A detailed overview of all reading scores and pairwise sequence comparison is provided in Tables 2 and 3.

Image quality Overall image quality was rated significantly higher for $rVIBE_{40}$ (4.4 ± 0.7) in axially oriented Gd-EOB-DTPA-enhanced scans as compared to $rVIBE_{100}$ (4.1 ± 0.7; p < 0.05) and cVIBE (4.0 ± 0.8; p < 0.05), whereas no significant differences could be observed in gadobutrol-enhanced examinations. In coronal multiplanar reformations both Gd-EOB-DTPA and gadobutrol-enhanced scans showed significantly higher reading scores for $rVIBE_{40}$ (p ≤ 0.001) in comparison to $rVIBE_{100}$. Pairwise comparison of $rVIBE_{40}$ versus cVIBE however only reached significant levels in Gd-EOB-DTPA-enhanced scans (p < 0.001) but not in gadobutrol-enhanced examinations. An image example of diagnostic

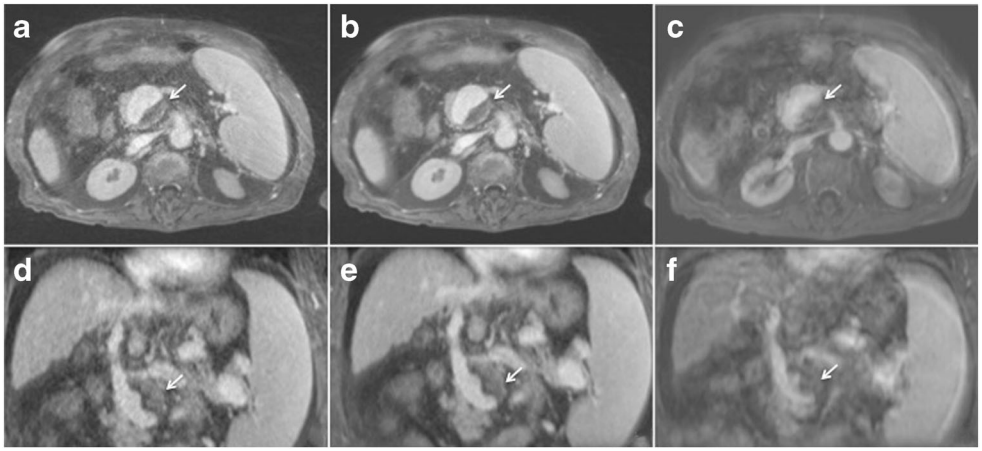

Fig. 2 Axial (**a** = $rVIBE_{40}$; **b** = $rVIBE_{100}$; **c** = cVIBE) and coronal reformations (**d** = $rVIBE_{40}$; **e** = $rVIBE_{100}$; **f** = cVIBE) of a 69-year-old patient with hepatocellular carcinoma. Images were acquired after administration of 10 ml gadobutrol. In radial VIBE acquisition (**a, b**), a subtotal thrombosis of the extra-hepatic portal vein is clearly visible (arrow) and not reliably detectable in the cVIBE (**c**). The same accounts for the coronal reformations. In this case, the cVIBE was rated non-diagnostic

image quality in all sequences is presented in Fig. 3. Exemplary images of Gd-EOB-DTPA and gadobutrol-enhanced scans are provided in Figs. 4 and 5.

Clarity and sharpness of hepatic vessels and liver edge were graded significantly higher for $rVIBE_{40}$ ($p < 0.001$) in comparison to $rVIBE_{100}$ and cVIBE in both axial and coronal planes of Gd-EOB-DTPA and gadobutrol-enhanced scans as demonstrated in Figs. 4 and 5.

Overall focal lesion conspicuity showed no significant differences among the observed sequences in gadobutrol-enhanced examinations ($p \geq 0.09$). In Gd-EOB-DTPA-enhanced scans in contrast, coronal multiplanar reformations revealed significantly higher lesion conspicuity in $rVIBE_{40}$ as compared to cVIBE ($p = 0.035$).

No significant differences could be observed in the depiction of the common bile duct and the biliary tree. For image examples refer to Fig. 3.

Artifacts Impairment of image quality due to sequence specific artefacts was most dominant for the radial sequences in axial planes and caused by streak artefacts, which occurred significantly stronger ($p < 0.001$) in $rVIBE_{40}$ as compared to $rVIBE_{100}$ in both gadobutrol- and Gd-EOB-DTPA-enhanced scans. In coronal multiplanar reformations artefacts due to motion were predominant with significantly lower artefacts ($p \leq 0.006$) in $rVIBE_{40}$ than in $rVIBE_{100}$ and cVIBE. An exemplary image is provided in Fig. 5.

Table 2 Results of qualitative image analysis for gadobutrol-enhanced examinations

Variables		$rVIBE_{40}$	$rVIBE_{100}$	cVIBE	Friedman-ANOVA *p*	$rVIBE_{40}$ vs. $rVIBE_{100}$ *p*	$rVIBE_{40}$ vs. cVIBE *p*	$rVIBE_{100}$ vs. cVIBE *p*
Image quality	ax	4.3 ± 0.8	4.1 ± 0.7	4.4 ± 0.6	0.050*	0.325	0.555	0.115
	cor	4.1 ± 0.8	3.2 ± 0.5	3.9 ± 0.5	<0.001	<0.001	0.294	0.003
Sharpness	ax	4.6 ± 0.6	3.8 ± 0.5	4.1 ± 0.5	<0.001	<0.001	0.001	0.101
	cor	4.3 ± 0.8	3.1 ± 0.5	3.6 ± 0.5	<0.001	<0.001	0.006	0.030
Lesion conspicuity	ax	4.7 ± 0.5	4.6 ± 0.8	4.8 ± 0.4	0.211	-	-	-
	cor	4.4 ± 1.3	4.1 ± 1.3	4.5 ± 0.8	0.089	-	-	-
Artifacts streak motion	ax	3.7 ± 0.7	4.5 ± 0.6	-	<0.001	<0.001	-	-
	cor	4.1 ± 0.8	3.4 ± 0.7	3.8 ± 0.6	0.006	0.007	0.393	0.066

Descriptive statistics and results of Friedman´s-ANOVA

ax axial, *cor* coronal planes

Table 3 Results of qualitative image analysis for Gd-EOB-DTPA-enhanced examinations

Variables		$rVIBE_{40}$	$rVIBE_{100}$	cVIBE	Friedman-ANOVA *p*	$rVIBE_{40}$ vs. $rVIBE_{100}$ *p*	$rVIBE_{40}$ vs. cVIBE *p*	$rVIBE_{100}$ vs. cVIBE *p*
Image quality	ax	4.4 ± 0.7	4.1 ± 0.7	4.0 ± 0.8	0.002	0.034	0.029	0.950
	cor	4.2 ± 0.8	3.3 ± 0.7	3.2 ± 0.9	<0.001	<0.001	<0.001	0.755
Sharpness	ax	4.6 ± 0.6	3.8 ± 0.5	3.9 ± 0.6	<0.001	<0.001	<0.001	0.238
	cor	4.2 ± 0.8	3.0 ± 0.7	3.3 ± 0.8	<0.001	<0.001	<0.001	0.169
Lesion conspicuity	ax	4.7 ± 0.7	4.8 ± 0.4	4.5 ± 1.1	0.010*	0.763	0.327	0.200
	cor	4.6 ± 0.8	4.7 ± 0.9	4.6 ± 0.9	0.004	0.291	0.035	0.291
Biliary tree	ax	4.7 ± 0.9	4.7 ± 0.9	4.6 ± 1.0	0.135	-	-	-
	cor	4.7 ± 0.9	4.3 ± 1.0	3.0 ± 1.3	0.368	-	-	-
Artifacts streak motion	ax	3.6 ± 0.6	4.1 ± 0.7	-	<0.001	0.001	-	-
	cor	3.9 ± 0.9	3.1 ± 0.7	3.5 ± 0.9	<0.001	<0.001	0.034	0.118

Descriptive statistics and results of Friedman´s-ANOVA. Friedman´s ANOVA indicates significant differences regarding lesion detection in axial planes*, however, in pairwise comparison it did not reach significant levels thus only indicating a trend

ax axial, *cor* coronal planes

Inter-reader agreement Analysis of kappa revealed a good inter-reader agreement for all observed parameters ($k \geq 0.65$; max. 0.94) and no significant differences between the sequences.

Quantitative image analysis

Image homogeneity Due to the reduced data reconstruction, coefficient of variation analysis showed the highest, i.e. most inhomogeneous, signal scores for the $rVIBE_{40}$ (0.05 ± 0.01) with significant differences to $rVIBE_{100}$ and cVIBE acquisition (0.03 ± 0.01 and 0.03 ± 0.00 respectively; $p < 0.001$). No significant differences could be found between the gadobutrol and Gd-EOB-DTPA subgroup. Further results of ANOVA analysis are provided in Table 4.

Liver-to-lesion contrast Analysis of liver-to-lesion contrast showed highest results for the cVIBE and lowest for the $rVIBE_{100}$ for all sequences acquired with significant differences of $rVIBE_{40}$ and cVIBE as compared to $rVIBE_{100}$ in the gadobutrol-subgroup ($p \leq 0.017$). In the Gd-EOB-DTPA subgroup no significant differences could be observed among the sequences ($p = 0.12$). Detailed results and results of the ANOVA analysis are provided in Table 4.

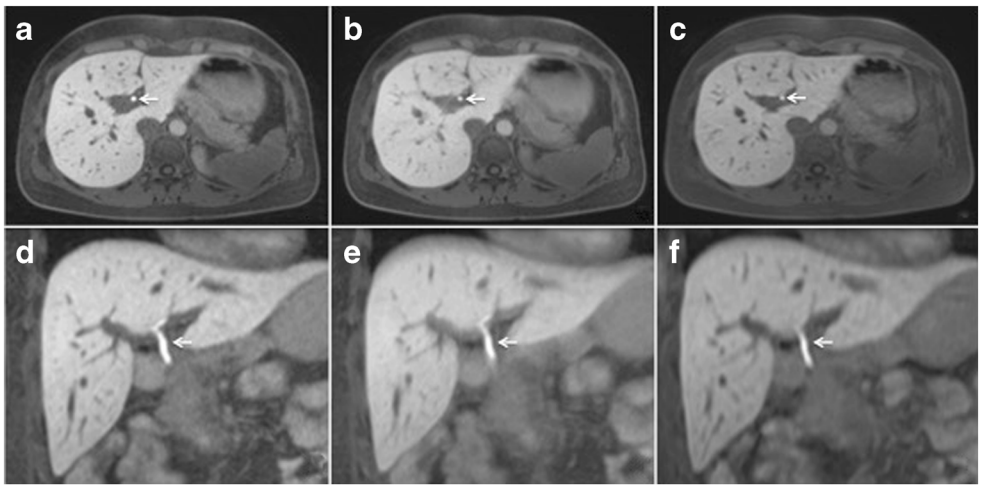

Fig. 3 Axial (**a** = $rVIBE_{40}$; **b** = $rVIBE_{100}$; **c** = cVIBE) and coronal (**d** = $rVIBE_{40}$; **e** = $rVIBE_{100}$; **f** = cVIBE) images of a 37-year-old patient to rule out pathological findings. Images were acquired 20 min after administration of 7 ml Gd-EOB-DPTA to rule out hepatic diseases. Image quality was rated excellent for all axial images and best for $rVIBE_{40}$ (**d**) in coronal multiplanar reformations. $rVIBE_{40}$ was also superior regarding sharpness and motion artifacts. Depiction of the common bile duct (arrow) was equally excellent in all images

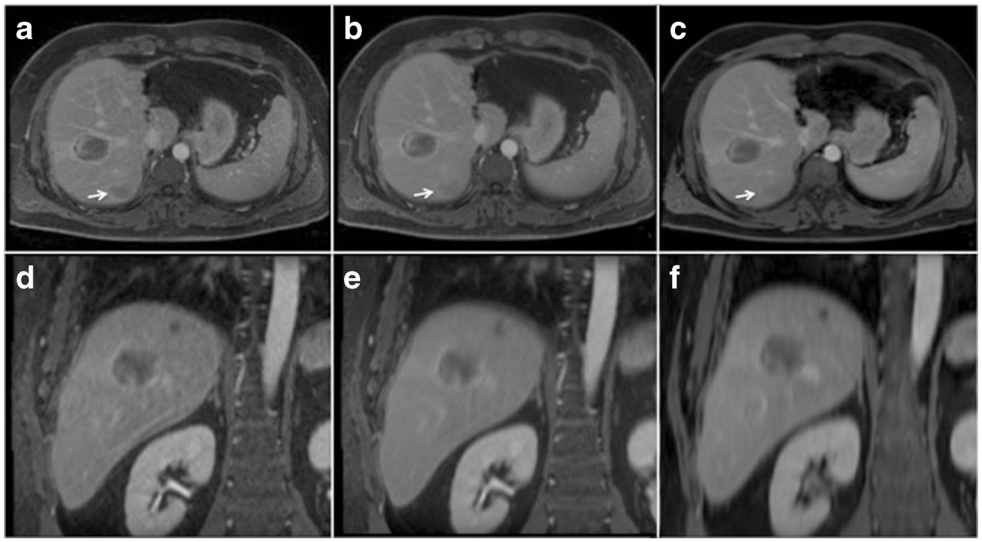

Fig. 4 Axial (**a** = $rVIBE_{40}$; **b** = $rVIBE_{100}$; **c** = cVIBE) and coronal (**d** = $rVIBE_{40}$; **e** = $rVIBE_{100}$; f = cVIBE) images of a 43-year-old patient with hepatic metastases of a rectum carcinoma. Images were acquired in a standard DCE liver protocol after administration of 10 ml gadobutrol. Sharpness was rated similar in the axial images and best in $rVIBE_{40}$ (**d**) acquisition in the coronal multiplanar reformations, clearly visible on the right kidney. Depiction of the lesion in segment V/VIII was equal for all sequences whereas the small lesion segment VI/VII (arrow) was best in $rVIBE_{40}$ (**a**), limited in $rVIBE_{100}$ (**b**) and not clearly detectable in the cVIBE (**c**)

Discussion

In this study we demonstrated that free-breathing self-gated 3D-isotropic radial VIBE significantly reduces artefacts due to motion and improves diagnostic image quality as compared to non-gated radial VIBE acquisitions and the standard Cartesian VIBE sequence. This applies in particular for coronal multiplanar reformations and late-phase Gd-EOB-DTPA-enhanced scans. Moreover, in 11 % of the cases only the radial VIBE provided sufficient image quality to detect relevant

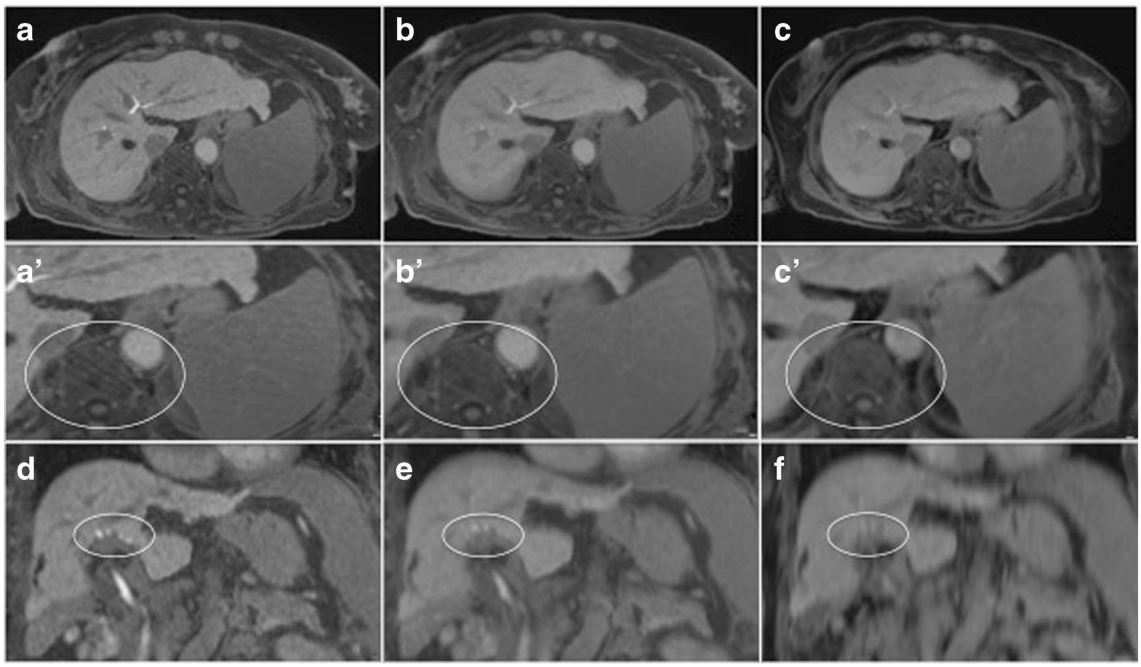

Fig. 5 Axial (**a** = $rVIBE_{40}$; **b** = $rVIBE_{100}$; c = cVIBE; enlarged **a´** = $rVIBE_{40}$; **b´** = $rVIBE_{100}$; **c´** = cVIBE) and coronal (**d** = $rVIBE_{40}$; **e** = $rVIBE_{100}$; **f** = cVIBE) images of a 74-year-old patient with hepatocellular carcinoma. Images were acquired 20 min after administration of 7 ml Gd-EOB-DTPA. Biliary tree depiction was rated similar in the axial planes. In coronal reformatted images, depiction was best in $rVIBE_{40}$ (**d**) and severely impaired in $rVIBE_{100}$ and cVIBE due to motion artefacts. Streak artefacts can be detected in the enlarged axial images (**a´**; **b´**; **c´**) and appear more pronounced in $rVIBE_{40}$ than in $rVIBE_{100}$ and are not visible in cVIBE

Table 4 Results of quantitative image analysis

Variables	$rVIBE_{40}$	$rVIBE_{100}$	cVIBE	Friedman-ANOVA		$rVIBE_{40}$ vs. $rVIBE_{100}$	$rVIBE_{40}$ vs. cVIBE	$rVIBE_{100}$ vs. cVIBE
				F	*p*	*p*	*p*	*p*
CV	0.05 ± 0.01	0.03 ± 0.01	0.03 ± 0.00	41.4	<0.001	<0.001	<0.001	1.000
Contrast^{g}	30.1 ± 15.6	21.8 ± 14.1	32.1 ± 7.7	8.8	0.001	0.001	1.000	0.017
Contrast$^{Gd\text{-}EOB}$	27.8 ± 10.4	23.1 ± 8.7	27.9 ± 13.4	2.2	0.119	-	-	-

Descriptive statistics and results of ANOVA-analysis for the observed sequences. Superscripted letters indicate subgroup analyses

CV coefficient of variation, *g* gadobutrol-enhaced, *Gd* Gd-EOB-DTPA-enhanced

pathologies or rule out unclear findings such as portal venous thrombosis or liver lesions.

These are important results for MR imaging of the liver, as patients with liver diseases are frequently unable to properly hold their breath, especially paediatric, elderly and severely ill patients, resulting in a considerable number of non-diagnostic examinations, although MR imaging would be the modality of choice [6, 25]. Therefore, based on our results we also consider free-breathing radial VIBE as a valuable approach for clinical routine to reduce the number of non-diagnostic abdominopelvic examinations due to motion-induced impairment of image quality. This data is consistent to the studies of Chandarana et al. [6, 8], who investigated abdominopelvic radial k-space sampling MRI in paediatric and adult patients showing comparable or improved image quality as compared to standard Cartesian VIBE in patients unable to adequately suspend their breath.

The improved robustness against patient movement of the assessed self-gated radial prototype sequence compared to the cVIBE allows acquisition of data during free breathing beyond an individual patient's breath-hold capability. Apart from a single case report [26], previous studies exploiting radial VIBE have used anisotropic voxel size [8, 27]. We also have optimized our scan protocol for a high isotropic resolution resulting in a prolonged acquisition time, which is, however, uncritical in late-phase acquisition. This facilitates arbitrary reformations of the 3D data set without additional reconstruction time and thus poses a viable strategy to improve the assessment of discreet anatomic and pathologic details. These findings are comparable to studies investigating 3D-MRI in musculoskeletal or brain imaging, where the 3D acquisition approach revealed improved image quality and diagnostic performance [19, 20, 22] due to improved delineation and depiction of complex and delicate anatomical structures.

A further significant improvement of the utilized prototype sequence was the implementation of a retrospective self-gating algorithm allowing for reduced image blurriness. This self-gating approach requires neither external physiological sensors nor the additional acquisition of an MRI navigator signal. Initial promising results evaluating this self-gating approach have already been published by Grimm et al. [17], who demonstrated improved lesion quantification in PET-MR examinations. These results are in accordance with our analysis as we found significantly improved image sharpness and artefact reduction with utilization of the self-gating algorithm. This might be especially useful for the assessment of small liver lesions and the bile ducts. However, this assumption could not be emphasized by statistically significant results in our study given that image quality of the non-gated radial and standard Cartesian VIBE was already excellent in most of the examinations. Further, more focused research in a dedicated patient sample with insufficient breath-hold capabilities is necessary to clarify this point.

The improved motion robustness of the radial k-space readout comes at the cost of increased streak artefacts caused by data inconsistencies due to undersampling and motion [8, 25]. The most severe artefacts were detected in the $rVIBE_{40}$ acquisition in axial planes. This can be explained by the fact that only 40 % of the acquired data were used for image reconstruction. By increasing the number of radial views and/or the gating acceptance rate, artefact severity can be decreased. Moreover, streak artefacts can be further reduced by deactivating coils distant to the actual region of interest since they decisively contribute to the increasing noise and enhance the artefact appearance [10, 28]. However, although streak artefacts impaired image quality in some cases, their optical impression was more like an added overlaying image texture than an image-ruining artefact [25]. At the same time, especially in coronal reformations, motion artefacts were significantly reduced in rVIBE acquisition. This is important since motion artefacts, in contrast to streak artefacts, have the potential to totally obscure relevant findings, just like ghosting or fold-over artefacts, which can also occur in Cartesian but not in radial k-space sampling [29].

The comparison of gadobutrol- versus Gd-EOB-DTPA-enhanced scans regarding the observed parameters in general revealed no significant differences between the contrast agents. However, in the Gd-EOB-DTPA sub-analysis the overall image quality of $rVIBE_{40}$ was rated significantly superior in comparison to the other sequences, presumably due

to the higher signal of liver parenchyma in the Gd-EOB-DTPA equilibrium phase as compared to gadobutrol-enhanced scans. Several studies have demonstrated the additional diagnostic value of hepatocyte-specific contrast agents for improved evaluation of liver lesions and assessment of tumour aggressiveness and outcome [30–34].

The major current disadvantage of radial k-space sampling is the relatively long acquisition time as compared to the standard Cartesian k-space readout, due to the reduced sampling efficiency and the lack of a parallel imaging acquisition. This makes it impossible to acquire arterial phase images, although the assessment of the arterial enhancement pattern of liver lesions stays crucial for an adequate dignity evaluation, particularly of HCC [1, 35]. To facilitate diagnostic image quality in multi-phase DCE-MRI including the arterial phase, different image reconstruction approaches have been developed recently, including k-space-weighted image contrast reconstruction (rVIBE-KWIC) [36, 37] or extra-dimensional golden-angle radial sparse parallel MRI reconstruction (XD-GRASP) [27].

Some limitations of this study need to be addressed. As mentioned above, acquisition time of the radial VIBE was too long to cover the arterial phase adequately. Consequently it was impossible to study the arterial enhancement pattern of liver lesions and, thus, an actual comparison to the cVIBE was only possible in the late-phase (gadobutrol) or hepatocyte-specific phase (Gd-EOB-DTPA). However, the primary aim of this study was to assess image quality and lesion conspicuity in late-phase examinations regardless of their arterial enhancement pattern. Still, the acquisition of an additional arterial phase (e.g. cVIBE arterial phase + rVIBE late phase) remains substantial in clinical routine for an adequate lesion evaluation. Moreover, due to the different sampling trajectories and spatial resolutions, acquisition parameters of the radial VIBE and the Cartesian VIBE did not completely match. As mentioned above, isotropic data acquisition of the axial cVIBE could not be obtained with adequate signal and sufficiently short acquisition time, with the consequence that spatial resolution and image quality of coronal reformations are method-related impaired as compared to the isotropic data of the radial VIBE. However, we still consider the possibility of reconstructing arbitrary multiplanar reformations as a notifiable benefit of rVIBE, as stated above, since cVIBE does not offer this approach, whether intended or not.

In conclusion, we demonstrated that utilization of free-breathing self-gated 3D-isotropic radial VIBE for liver imaging provides significantly reduced motion artefacts and superior image quality as compared to a standard Cartesian VIBE acquisition, especially in multiplanar reformations and Gd-EOB-DTPA-enhanced hepatocyte-specific late-phase examinations.

Acknowledgments The scientific guarantor of this publication is Mike Notohamiprodjo. The authors of this manuscript declare relationships with the following companies: Robert Grimm is an employee of Siemens Healthcare and was involved in the development of the self-gating algorithm. The authors state that this work has not received any funding. No complex statistical methods were necessary for this paper.

Institutional Review Board approval was obtained. Written informed consent was waived by the Institutional Review Board. Methodology: retrospective, performed at one institution.

References

1. Elsayes KM, Narra VR, Yin Y, Mukundan G, Lammle M, Brown JJ (2005) Focal hepatic lesions: diagnostic value of enhancement pattern approach with contrast-enhanced 3D gradient-echo MR imaging. Radiographics 25:1299–1320
2. Rofsky NM, Lee VS, Laub G et al (1999) Abdominal MR imaging with a volumetric interpolated breath-hold examination. Radiology 212:876–884
3. Hecht EM, Holland AE, Israel GM et al (2006) Hepatocellular carcinoma in the cirrhotic liver: gadolinium-enhanced 3D T1-weighted MR imaging as a stand-alone sequence for diagnosis. Radiology 239:438–447
4. Wood ML, Henkelman RM (1985) MR image artifacts from periodic motion. Med Phys 12:143–151
5. Ehman RL, McNamara MT, Brasch RC, Felmlee JP, Gray JE, Higgins CB (1986) Influence of physiologic motion on the appearance of tissue in MR images. Radiology 159:777–782
6. Chandarana H, Block KT, Winfeld MJ et al (2014) Free-breathing contrast-enhanced T1-weighted gradient-echo imaging with radial k-space sampling for paediatric abdominopelvic MRI. Eur Radiol 24:320–326
7. Noterdaeme O, Gleeson F, Phillips RR, Brady M (2007) Quantification of missing and overlapping data in multiple breath hold abdominal imaging. Eur J Radiol 64:273–278
8. Chandarana H, Block TK, Rosenkrantz AB et al (2011) Free-breathing radial 3D fat-suppressed T1-weighted gradient echo sequence: a viable alternative for contrast-enhanced liver imaging in patients unable to suspend respiration. Invest Radiol 46:648–653
9. Lauterbur PC (1989) Image formation by induced local interactions. Examples employing nuclear magnetic resonance. 1973. Clin Orthop Relat Res 3–6.
10. Block KT, Chandarana H, Milla S et al (2014) Towards routine clinical use of radial stack-of-stars 3d gradient-echo sequences for reducing motion sensitivity. J Korean Soc Magnet Resonance Med 18:87–106
11. Chandarana H, Feng L, Block TK et al (2013) Free-breathing contrast-enhanced multiphase MRI of the liver using a combination of compressed sensing, parallel imaging, and golden-angle radial sampling. Invest Radiol 48:10–16
12. Azevedo RM, de Campos RO, Ramalho M, Heredia V, Dale BM, Semelka RC (2011) Free-breathing 3D T1-weighted gradient-echo sequence with radial data sampling in abdominal MRI: preliminary observations. AJR Am J Roentgenol 197:650–657
13. Bangiyev L, Raz E, Block TK et al. (2015) Evaluation of the orbit using contrast-enhanced radial 3D fat-suppressed T weighted gradient echo (Radial-VIBE) sequence. Br J Radiol 20140863.
14. Chandarana H, Heacock L, Rakheja R et al (2013) Pulmonary nodules in patients with primary malignancy: comparison of hybrid PET/MR and PET/CT imaging. Radiology 268:874–881
15. Shankaranarayanan A, Simonetti OP, Laub G, Lewin JS, Duerk JL (2001) Segmented k-space and real-time cardiac cine MR imaging with radial trajectories. Radiology 221:827–836

16. Bamrungchart S, Tantaway EM, Midia EC et al (2013) Free breathing three-dimensional gradient echo-sequence with radial data sampling (radial 3D-GRE) examination of the pancreas: Comparison with standard 3D-GRE volumetric interpolated breathhold examination (VIBE). J Magn Reson Imaging 38:1572–1577
17. Grimm R, Furst S, Souvatzoglou M et al (2015) Self-gated MRI motion modeling for respiratory motion compensation in integrated PET/MRI. Med Image Anal 19:110–120
18. Furst S, Grimm R, Hong I et al (2015) Motion correction strategies for integrated PET/MR. J Nucl Med 56:261–269
19. Xiao L, Siu CW, Yeung K, Leung A, Yuen MK, Wong YC (2015) MRI of the cervical spine with 3D gradient echo sequence at 3T: initial experience. Clin Radiol 70:926–931
20. Gustas CN, Blankenbaker DG, Rio AM, Winalski CS, Kijowski R (2015) Evaluation of the Articular Cartilage of the Knee Joint Using an Isotropic Resolution 3D Fast Spin-Echo Sequence With Conventional and Radial Reformatted Images. AJR Am J Roentgenol 205:371–379
21. AlObaidy M, Ramalho M, Busireddy KK et al (2015) High-resolution 3D-GRE imaging of the abdomen using controlled aliasing acceleration technique - a feasibility study. Eur Radiol
22. Notohamiprodjo M, Kuschel B, Horng A et al (2012) 3D-MRI of the ankle with optimized 3D-SPACE. Invest Radiol 47:231–239
23. van Elmpt W, Hamill J, Jones J, De Ruysscher D, Lambin P, Ollers M (2011) Optimal gating compared to 3D and 4D PET reconstruction for characterization of lung tumours. Eur J Nucl Med Mol Imaging 38:843–855
24. Dietrich O, Raya JG, Reeder SB, Reiser MF, Schoenberg SO (2007) Measurement of signal-to-noise ratios in MR images: influence of multichannel coils, parallel imaging, and reconstruction filters. J Magn Reson Imaging 26:375–385
25. Reiner CS, Neville AM, Nazeer HK et al (2013) Contrast-enhanced free-breathing 3D T1-weighted gradient-echo sequence for hepatobiliary MRI in patients with breath-holding difficulties. Eur Radiol 23:3087–3093
26. Rosenkrantz AB, Block TK, Hindman N, Vega E, Chandarana H (2014) Combination of increased flip angle, radial k-space trajectory, and free breathing acquisition for improved detection of a biliary variant at living donor liver transplant evaluation using gadoxetic acid-enhanced MRCP. J Comput Assist Tomogr 38:277–280
27. Chandarana H, Feng L, Ream J et al (2015) Respiratory Motion-Resolved Compressed Sensing Reconstruction of Free-Breathing Radial Acquisition for Dynamic Liver Magnetic Resonance Imaging. Invest Radiol
28. Xue Y, Yu J, Kang HS, Englander S, Rosen MA, Song HK (2012) Automatic coil selection for streak artifact reduction in radial MRI. Magn Reson Med 67:470–476
29. Schultz CL, Alfidi RJ, Nelson AD, Kopiwoda SY, Clampitt ME (1984) The effect of motion on two-dimensional Fourier transformation magnetic resonance images. Radiology 152:117–121
30. Zech CJ, Grazioli L, Breuer J, Reiser MF, Schoenberg SO (2008) Diagnostic performance and description of morphological features of focal nodular hyperplasia in Gd-EOB-DTPA-enhanced liver magnetic resonance imaging: results of a multicenter trial. Invest Radiol 43:504–511
31. Kwon HJ, Byun JH, Kim JY et al (2015) Differentiation of small (</=2cm) hepatocellular carcinomas from small benign nodules in cirrhotic liver on gadoxetic acid-enhanced and diffusion-weighted magnetic resonance images. Abdom Imaging 40:64–75
32. Choi JW, Lee JM, Kim SJ et al (2013) Hepatocellular carcinoma: imaging patterns on gadoxetic acid-enhanced MR Images and their value as an imaging biomarker. Radiology 267:776–786
33. Park HJ, Jang KM, Kang TW et al (2015) Identification of Imaging Predictors Discriminating Different Primary Liver Tumours in Patients with Chronic Liver Disease on Gadoxetic Acid-enhanced MRI: a Classification Tree Analysis. Eur Radiol. doi:10.1007/s00330-015-4136-y
34. Kim YS, Song JS, Lee HK, Han YM (2015) Hypovascular hypointense nodules on hepatobiliary phase without T2 hyperintensity on gadoxetic acid-enhanced MR images in patients with chronic liver disease: long-term outcomes and risk factors for hypervascular transformation. Eur Radiol. doi:10.1007/s00330-015-4146-9
35. Quillin SP, Atilla S, Brown JJ, Borrello JA, Yu CY, Pilgram TK (1997) Characterization of focal hepatic masses by dynamic contrast-enhanced MR imaging: findings in 311 lesions. Magn Reson Imaging 15:275–285
36. Fujinaga Y, Ohya A, Tokoro H et al (2014) Radial volumetric imaging breath-hold examination (VIBE) with k-space weighted image contrast (KWIC) for dynamic gadoxetic acid (Gd-EOB-DTPA)-enhanced MRI of the liver: advantages over Cartesian VIBE in the arterial phase. Eur Radiol 24:1290–1299
37. Fujinaga Y, Kitou Y, Ohya A et al (2015) Advantages of radial volumetric breath-hold examination (VIBE) with k-space weighted image contrast reconstruction (KWIC) over Cartesian VIBE in liver imaging of volunteers simulating inadequate or no breath-holding ability. Eur Radiol. doi:10.1007/s00330-015-4103-7